PURPOSE-LED PUBLISHING™

PAPER • OPEN ACCESS

Magnetic compensation in sputtered ferrimagnetic $Mn_{4-x}Ga_xN$ thin films

To cite this article: L Prendeville *et al* 2024 *J. Phys. D: Appl. Phys.* **57** 355005

View the article online for updates and enhancements.

The Electrochemical Society
Advancing solid state & electrochemical science & technology

ECS UNITED

247th ECS Meeting
Montréal, Canada
May 18-22, 2025
Palais des Congrès de Montréal

Abstracts due December 6th

Showcase your science!

Magnetic compensation in sputtered ferrimagnetic $Mn_{4-x}Ga_xN$ thin films

L Prendeville[1] , **P Jiménez-Cavero**[1,4] , **A Naden**[2] , **Yangkun He**[1,3] , **K Rode**[1] ,
Z Gercsi[1] **and J M D Coey**[1,*]

[1] Centre for Research on Adaptive Nanostructures and Nanodevices, Trinity College Dublin, Dublin, Ireland
[2] School of Chemistry, University of St Andrews, St Andrews, United Kingdom
[3] School of Materials Science and Engineering, Beihang University, Beijing 100191, People's Republic of China

E-mail: jcoey@tcd.ie

CrossMark

Abstract

Fully compensated ferrimagnets are attracting increasing attention for spintronics. Here we report a series of $Mn_{4-x}Ga_xN$ ferrimagnetic thin films grown on (100)-oriented MgO by magnetron sputtering. A small tetragonal distortion with $c/a = 0.99$ leads to perpendicular magnetic anisotropy with a [001] easy axis. The magnetisation decreases with increasing Ga content up to $x = 0.18$, where the magnetic moment is close to zero at room temperature. It increases with further increase of x, indicating the magnetic compensation composition has been crossed and the dominant sublattice has switched from Mn on the corner sites, where it is progressively replaced by nonmagnetic Ga, to noncollinear Mn on the face-centered sites. Compensation found at 235 K in a remanent scan of the $x = 0.18$ film is confirmed by measurements of the anomalous Hall effect and interpolation of the inverse coercivity. This work establishes the conditions for thin film growth of $Mn_{4-x}Ga_xN$ that could be used for room-temperature ferrimagnetic spintronics. The behaviour of thin films is compared with that of bulk material.

1. Introduction

The study of compensated metallic ferrimagnets for spintronic applications is a topic of growing interest [1–3]. Ferrimagnets combine some of the properties of ferromagnets with some of antiferromagnets. Like a ferromagnet they can be manipulated by an external magnetic field but they exhibit the fast spin dynamics of antiferromagnetic systems when close to

compensation [4]. Even at the magnetic compensation point, it is still possible to measure magnetisation via the anomalous Hall effect (AHE) because the two sublattices make unequal and opposite contributions to the resultant effect. There is some evidence for a topological Hall effect in Mn_4N thin films [5]. Mn_4N is a Q-type ferrimagnet and has advantages including a high ferrimagnetic Néel temperature of 780 K in the bulk [6]. In the pure form there is no sign of compensation in either bulk or thin films [5, 7], but compensation can be realised by atomic substitution for Mn, $Mn_{4-x}Z_xN$, not only by nonmagnetic atoms [8] but also by Z = Co and Ni [4, 9, 10]. No compensation is found for Z = Cr and Fe because these dopant atoms occupy both corner and face-centered sites with no particular preference [11]. In the case of In substitution, a ferrimagnetic-ferromagnetic phase transition was reported between $x = 0.15$ and $x = 0.27$ based on AHE measurements

[4] Current address: Centro Universitario de la Defensa de Zaragoza, Spain.
[*] Author to whom any correspondence should be addressed.

and first principles calculations [12]. There has also been a recent study by Sakaguchi *et al* on the transport and optical properties of boron doped Mn_4N thin films, where the boron atoms occupy interstitial sites at the center of the unit cell [13].

In bulk form Mn_4N has a face centered cubic Mn structure with a N atom at the 1b body-center position. There are two Mn sublattices, the cube corner 1a sites and the face center 3c sites, which form kagome lattices in the {111} planes. The unequal sublattices couple antiferromagnetically yielding a net moment of 1.1 μ_B/f.u. at low temperature with very weak $\langle 111 \rangle$ anisotropy, $K_1 \approx 1.5$ kJm^{-3} [7]. The moment m_{1a} of each 1a Mn lies along [111] while the 3c sublattice has a more complex noncollinear character due to frustration of the antiferromagnetic nearest-neighbour 3c–3c interactions. The resultant triangular ferrimagnetic spin structure is illustrated in figure 1(a); the Mn 3c moments, m_{3c}, form an umbrella-like configuration, where individual moments have a component in the (111) plane at an angle of 120° to each other, with a resultant moment along [$\bar{1}\bar{1}\bar{1}$]. This noncollinear spin structure was first detected in a polarised neutron diffraction study by Fruchart *et al* [14] and supported by the calculations of Uhl *et al* [15] who found a tilt angle of $\theta = 15°$ between m_{3c} and the [111] easy direction, in accord with the neutron data. Experimental values for m_{1a} and m_{3c} were 3.80 μ_B/f.u. and 0.9 μ_B/f.u. while the calculations found values of 3.45 μ_B/f.u. and 0.96 μ_B/f.u. [14, 15]. More recent DFT calculations of bulk material [6] found a similar m_{1a} of 3.65 μ_B/f.u. but a greater m_{3c} of 2.35 μ_B/f.u. and a larger tilt angle of $\theta = 70°$. However, Zhang *et al* also found that the canting angle θ can vary with the magnitude of both m_{1a} and m_{3c} while the net moment of 1.24 μ_B/f.u. is maintained. This is close to the value of 1.17 μ_B/f.u. from magnetisation measurements at 4.2 K [14].

When grown as a thin film on (100)-oriented single crystal substrates such as Si, MgO, $SrTiO_3$, $LaAlO_3$ or $(LaAlO_3)_{0.3}(Sr_2TaAlO_6)_{0.7}$, Mn_4N experiences an in-plane biaxial strain and becomes slightly tetragonal with a c/a ratio of ≈ 0.99 [16–19]. The films are not epitaxial as the tensile strain is similar on different substrates. They exhibit perpendicular magnetic anisotropy (PMA) and develop coercivity as the easy direction shifts from [111] in the bulk to [001] in the films. The thin films have a lower magnetic moment of approximately 0.5–0.6 μ_B/f.u [5] at room temperature in comparison to the bulk value of 0.75–0.81 μ_B/f.u. [6, 14], but there is no compensation and the magnetic ordering temperature is ≈ 750 K [5]. The PMA and [001] easy axis imply a change of the noncollinear magnetic spin structure from the bulk version. He *et al* [5] considered the spin structure of tetragonal bulk Mn_3ZN perovskites with $Z =$ Cu and Rh, and proposed the 'bulk like' configuration shown in figure 1(b) as most likely for the thin films, which preserves the noncollinearity of the face centered Mn sites, shows PMA and complies with the signs of the distance-dependent exchange interactions between Mn atoms. The tetragonal distortion splits the original Mn 3c sublattice into two separate sublattices, Mn 1c and 2e, with tilt angles of δ and γ from the easy axis. Recent reviews on Mn_4N-based films and heterostructures [20–22] outline some potential opportunities for the use of this material in spintronics.

Compensation in Mn_4N has been claimed, based on calculations that assumed a collinear three-sublattice magnetic structure [24], for which there is no experimental evidence [25]. The magnetisation versus temperature curve is Q-type since $m_{1a} > 3\langle m_{3c}\rangle$ for all temperatures below T_c. Nevertheless it is expected that by doping thin film Mn_4N with elements that replace Mn atoms at 1a sites it should be possible to achieve compensation as was shown by Zhang *et al* for doped bulk Mn_4N with a range of different elements including $Z =$ Ga, which exhibits compensation at $x = 0.26$ and was regarded as most suitable [6]. The aim of this work was therefore to grow and characterise $Mn_{4-x}Ga_xN$ thin films. A series of samples with x ranging from 0 to 0.27 was prepared by magnetron sputtering, a versatile deposition technique offering many advantages in terms of cost, time and scalability. Their structural, magnetic and magneto-transport properties are characterised.

2. Methodology

2.1. Experimental measurements

The $Mn_{4-x}Ga_xN$ thin films were grown on 10 mm × 10 mm × 0.5 mm (100) MgO substrates by DC magnetron sputtering. All were co-sputtered from one or two Mn targets and a Mn_3Ga target in the presence of N_2, where x was varied by altering the current in the Mn guns. In all cases the ratio of Ar:N_2 during the deposition was 20:1 and substrate temperatures ranged between 390 °C and 440 °C, depending on the composition. A mask was placed in front of the substrate in the holder to prevent any side-wall deposition which can result in the observation of unusual features in magnetometry measurements [26]. The films were cooled in the presence of N_2, a necessary step for formation of the correct phase, and capped with SiO_2 to prevent oxidation. See table 1 for details of the conditions used for each composition. All films were structurally characterised by x-ray diffraction (XRD) and x-ray reflectivity (XRR) using a Panalytical X'Pert Pro diffractometer with Cu K_α radiation, $\lambda = 0.154\ 06$ nm. Reciprocal space mapping (RSM) was also performed on each composition using a Bruker D8 Discover diffractometer. The samples were then cut into four pieces of approximate area 5 mm × 5 mm using a diamond pen. One piece of each composition was mounted into a gelcap straw and and magnetisation measurements were performed using a 5 T Quantum Design SQUID magnetometer.

Cross-sections for (scanning) transmission electron microscopy (S)TEM were prepared by focused ion beam milling on an FEI Scios with bulk milling at an acceleration voltage of 30 kV followed by final polishing at 2 kV. STEM measurements were performed on an FEI Titan Themis operated at 200 kV, equipped with a CEOS DCOR probe corrector, a SuperX energy dispersive x-ray spectrometer (EDX) and a Gatan Enfinium electron energy loss (EEL) spectrometer. High angle annular dark field (HAADF) images were acquired with a probe convergence angle of 20 mrad and
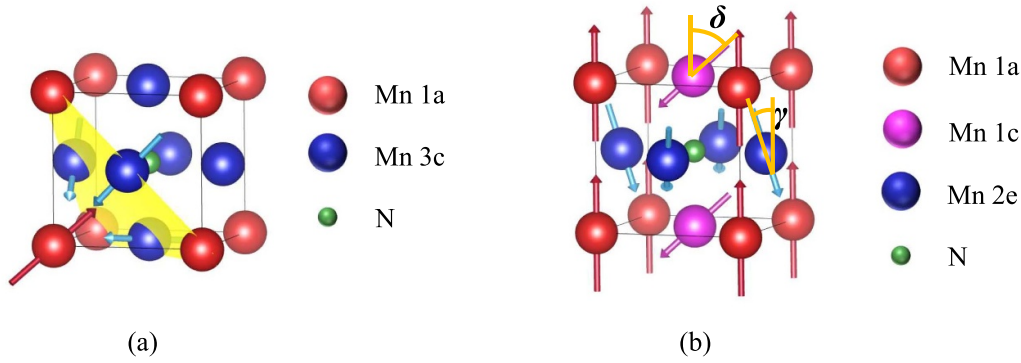
J. Phys. D: Appl. Phys. **57** (2024) 355005

L Prendeville *et al*

Figure 1. (a) The spin structure of bulk Mn$_4$N with the 1a and 3c sublattices depicted by red and blue spheres respectively. A (111) plane is highlighted in yellow. (b) The proposed spin structure of thin-film Mn$_4$N on (100) MgO, which exhibits perpendicular magnetic anisotropy. The angles δ and γ are relative to [001]. Adapted figure with permission from [5], Copyright (2022) by the American Physical Society and drawn using Vesta [23].

Table 1. Details of the deposition conditions used to grow films of Mn$_{4-x}$Ga$_x$N, including substrate temperature during deposition (T_{dep}) and the rate of N$_2$ flow into the chamber as the sample cooled (S_{N_2}) as well as the resulting film thicknesses (t), the obtained a and c parameters from RSM measurements and their ratio.

Composition	T_{dep} (°C)	S_{N_2} (sccm)	t (nm)	a (nm)	c (nm)	c/a
Mn$_4$N	440	2.6	30.8	0.389	0.386	0.992
Mn$_{3.91}$Ga$_{0.09}$N	440	2.3	30.5	0.391	0.386	0.987
Mn$_{3.89}$Ga$_{0.11}$N	425	2.1	24.2	0.390	0.386	0.990
Mn$_{3.87}$Ga$_{0.13}$N	425	2.3	25.2	0.390	0.386	0.990
Mn$_{3.86}$Ga$_{0.14}$N	390	2.4	22.6	0.391	0.386	0.987
Mn$_{3.82}$Ga$_{0.18}$N	410	1.6	31.6	0.389	0.385	0.990
Mn$_{3.80}$Ga$_{0.20}$N	390	1.9	26.1	0.390	0.385	0.987
Mn$_{3.73}$Ga$_{0.27}$N	390	1.5	35.0	0.391	0.387	0.990

inner/outer collection angles of 91 and 200 mrad, respectively. EEL spectra were acquired with a collection angle of 8.1 mrad.

All AHE measurements were performed at room temperature in an out-of-plane configuration with a 5.5 T superconducting magnet. Samples were patterned into triple Hall crosses (8-legged Hall bars) of length 50 μm and width 10 μm by 2-step UV lithography followed by a metallisation step for the contact pads. Magneto-transport and magnetometry experiments were thus performed on different physical samples but they had been grown under the same deposition conditions for each composition.

3. Results and discussion

3.1. Structural characterisation

XRD patterns confirmed the growth of crystalline Mn$_{4-x}$Ga$_x$N thin films on MgO in the case of all compositions, as shown in figure 2(a). In all but one of the films Laue fringes can be observed on the (002) Mn$_4$N peak at $2\theta \sim 47°$, which indicate well-oriented (001) films of high crystalline quality [27]. The small broad peak at $2\theta \approx 41°$ shows that a minor amount of α-Mn was present in three of the films, Mn$_{3.91}$Ga$_{0.09}$N, Mn$_{3.89}$Ga$_{0.11}$N, and Mn$_{3.73}$Ga$_{0.27}$N. In the case of Mn$_{3.73}$Ga$_{0.27}$N a larger amount of this parasitic phase was formed. For completeness and comparison, results from this

sample are included here, but it is likely that the Ga-doping is slightly higher than the nominal $x = 0.27$. The lattice parameter of bulk Mn$_4$N has been reported as 386.5 pm [6, 28], which is smaller than the a-axis deduced for each of the films from RSM measurements. This indicates that the material undergoes a tensile strain at the interface with the MgO substrate. The lattice mismatch of 8.2% results in a non-epitaxial tetragonal distortion of the films. Figure 2(b) shows one RSM plot for Mn$_{3.87}$Ga$_{0.13}$N which was obtained by carrying out an $\omega - 2\theta$ scan around the (113) MgO peak. ω is the angle between the incoming x-rays and the sample surface while θ refers to the Bragg angle. The low intensity Mn$_4$N (113) peak is close enough to the MgO to apply the same corrections to extract accurate a and c values for the film. RSM measurements on all films confirmed the tetragonal distortion as the c/a ratio of out-of-plane to in-plane lattice parameters was 0.99 in each case, see table 1. Film thicknesses ranged from 22 to 35 nm and were determined by fitting the low-angle x-ray scattering data of figure 2(c). In each case it was necessary to include a thin (of order 1–2 nm) layer of MnO above and below the Mn$_{4-x}$Ga$_x$N layer to achieve an acceptable XRR fit. It is not uncommon to observe such oxide formation at Mn interfaces [17, 29–31]. Li *et al* also showed that it is possible to grow Mn$_4$N thin films with PMA on glass substrates using a MnO seed layer [32]. The stack structure proposed from XRR where the Mn$_{4-x}$Ga$_x$N layer is bounded by a MnO layer at both interfaces is shown in figure 2(d).
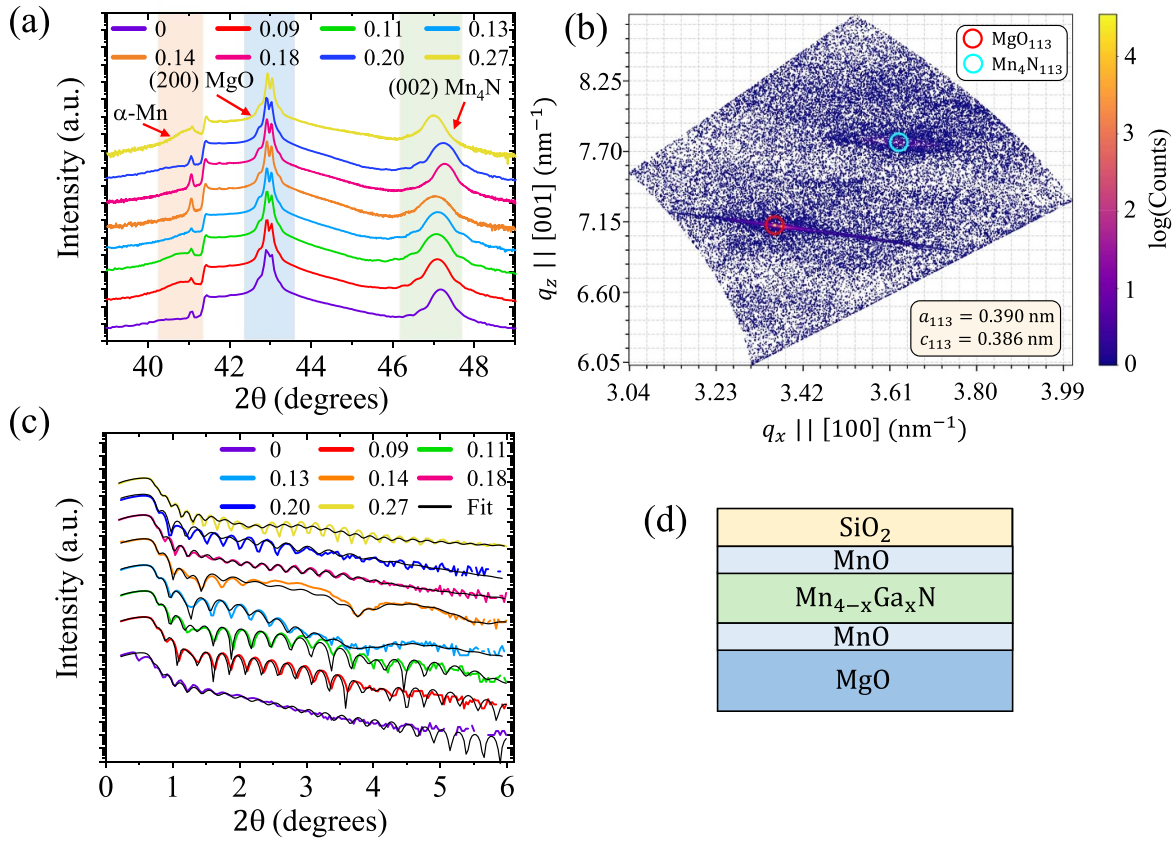
J. Phys. D: Appl. Phys. **57** (2024) 355005

L Prendeville *et al*

Figure 2. (a) XRD patterns for eight different $Mn_{4-x}Ga_xN$ compositions with x ranging from 0 to 0.27. The (002) Mn_4N peak is in the shaded green region of the graph while the orange and blue regions highlight peaks associated with α-Mn and the MgO substrate. (b) Reciprocal space map of $Mn_{3.87}Ga_{0.13}N$ around the MgO (113) peak, where q_x and q_z are reciprocal space vectors related to a and c by $\frac{\sqrt{2}}{q_x}$ and $\frac{3}{q_z}$ respectively. XRR data and fits are shown in (c) and the expected stack structure is given in (d).

A thin (≈ 20 nm) lamella was prepared from a $Mn_{3.87}Ga_{0.13}N$ film and STEM was performed to investigate the potential interfacial oxide layer and the local nanostructure within the films. A layer of carbon was deposited on the film to provide a good contrast for TEM imaging, followed by a Pt layer to hold the lamella in place. Figure 3 illustrates two HAADF STEM images of the bottom and top interfaces of the film aligned along the [100] zone axis. At both interfaces there are subtle contrast differences, potentially due to the interfacial oxide, which manifests itself as a slight blurring in this region. Based on XRR fitting we know that these regions are on the order of 1–2 nm.

To further investigate the interfacial MnO we collected EDX spectra across various regions of the stack and performed EEL spectroscopy around the Mn L edge and O K edge. Figure 4(a) shows a STEM image of the stack where the different colours highlight the regions where intensity from various elements including Mg, Si, Mn and Ga was collected. The blue line indicates the profile along which the EDX spectrum in (b) was collected. This spectrum shows a diffusion gradient of Mn into both the SiO_2 capping layer and the MgO substrate as well as an increasing oxygen content close to the interface. Intensity from oxygen is also picked up throughout the $Mn_{3.87}Ga_{0.13}N$ layer which probably comes from the brief

exposure of the surface to atmosphere as the lamella was transferred into the measurement system. The Ga content seems unvarying throughout the film and was 3.1% of the total Mn content, in agreement with the dopant calibration from XRR ($\frac{0.13}{4} \approx 3.3\%$). EEL spectra were taken at the top interface and middle section of the film and the intensity was normalised to the Mn L_3 edge, figure 4(c). The increased branching ratio $\frac{I_{L_2}}{I_{L_3}+I_{L_2}}$, where I_{L_2} and I_{L_3} are the integrated intensities of each edge, of the Mn 2p to 3d transition strongly suggests the presence of MnO (i.e. Mn^{2+}) at the top of the film [33]. The oxygen K edge peak is evident in both spectra but its intensity is slightly higher in the spectrum from the top interface. The selected area electron diffraction (SAD) pattern of the stack in figure 4(d) further highlights the cube-on-cube growth of Mn_4N on MgO. The central bright spot is from the direct beam while those circled in red are the family of {200} reflections from the MgO substrate. Smaller diffraction spots close to the higher intensity substrate-related spots come from the $Mn_{3.87}Ga_{0.13}N$ film.

3.2. Magnetic and magneto-transport properties

There are two sites on which Mn can be replaced by doping, 1a or 3c. Co tends to replace Mn at the 3c site and Fe, Cr
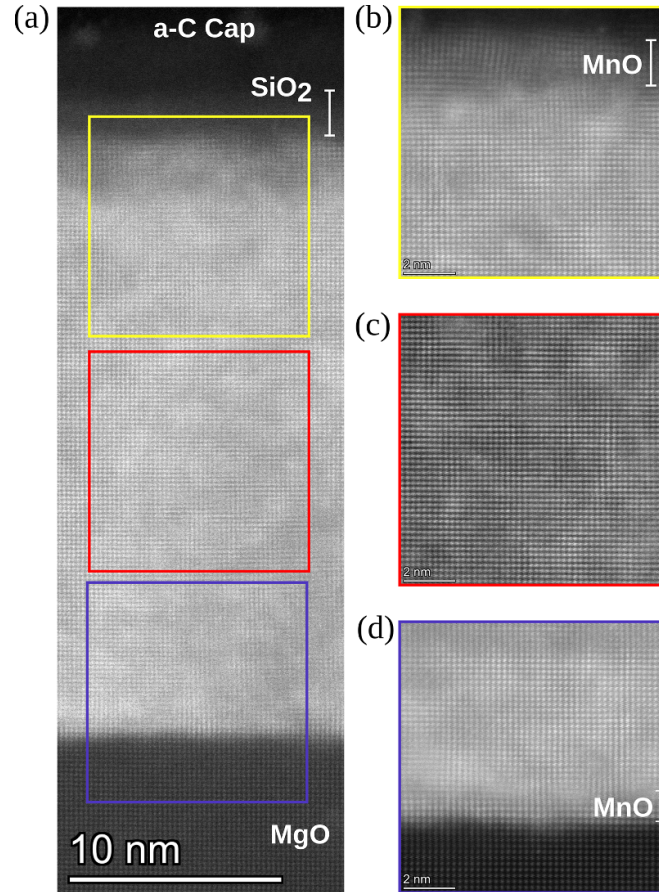
J. Phys. D: Appl. Phys. **57** (2024) 355005

L Prendeville *et al*

Figure 3. Atomic resolution HAADF STEM images illustrating the formation of MnO at the interfacial regions of $Mn_{3.87}Ga_{0.13}N$. (a) Shows the whole section throughout the film stack while (b)–(d) are higher magnification images of the top, middle and bottom regions.

and In have little preference [11, 12]. Zhang *et al* showed that Ga occupies 1a corner positions in the bulk material [6]. The rate of decrease of moment per formula unit there, $\frac{dm}{dx} = -3.7\,\mu_B$/Ga atom, agrees with the 1a-site Mn moment. Ga-doping is therefore a good way to induce compensation. Figure 5 shows out-of-plane room temperature SQUID hysteresis loops, illustrating the effects of increased Ga doping on the net ferrimagnetic magnetisation of the pure sample. The in-plane loop has also been plotted for $x = 0$, indicating an anisotropy field $\mu_0 H_a$ of 2.3 T and a corresponding perpendicular anisotropy constant K_1 of 100 kJm^{-3}. Four of the curves ($x = 0.09, 0.11, 0.13, 0.20$) exhibited a wasp waist due to hard and soft magnetic contributions to the loop. Li *et al* attributed a wasp waist in their $Mn_{4-x}Gd_xN$ films to antiferromagnetic interactions [34] while Komori *et al* associated kinks close to zero field in the magnetisation loops of Ni-doped Mn_4N to a mixture of hard and soft magnetic phases [9]. From our EDX spectra we know that we have an interfacial oxide layer but there is also the possibility that a build-up of excess Ga in these regions could contribute to the soft component. For Ga-doped films we observed a decrease in the saturation magnetisation with increasing Ga content up to $x = 0.18$ and the coercivity of the hard component of each loop increased as more Ga was added up to $x = 0.14$ where only the soft component was visible. The magnetisation was close to zero at room temperature for $x = 0.18$ where the measurement showed no

trace of a loop, a good sign that we were close to compensation and the coercivity would be greater than 5 T. With further increases in Ga content, signs of coercivity started to appear and it decreased again as the saturation magnetisation began to increase.

The average high-field magnetisation is plotted as a function of Ga content in figure 6(a), with negative values for samples with $x = 0.20$ and 0.27 which are above their compensation points at room temperature. Fitting a straight line to this plot yields a slope with $\frac{dm}{dx} = -3.1 \pm 0.4\,\mu_B$/Ga, indicating that the moment of the system decreases by this amount with the addition of each dopant Ga atom. This is slightly lower than the calculated slope in [6] for the bulk equivalent but is still close to the expected moment on the Mn 1a sites. This is further evidence that Ga atoms replace only Mn 1a rather than 3c sites in thin films, just as they also do in bulk. It provides support for a rigid-band model where the magnitude and direction of the neighbouring Mn 1a and 3c spins as well as the exchange between them are all unaffected by addition of Ga. The x-intercept of this plot predicts compensation close to room temperature is achieved in $Mn_{4-x}Ga_xN$ for $x = 0.20 \pm 0.03$, which is lower than the value of $x = 0.26$ measured in the bulk [6]. We know that compensation must be close to $x = 0.18$ from the room temperature magnetisation hysteresis loops. The difference between the bulk and film compensation compositions can be related to the lower ferrimagnetic moment in
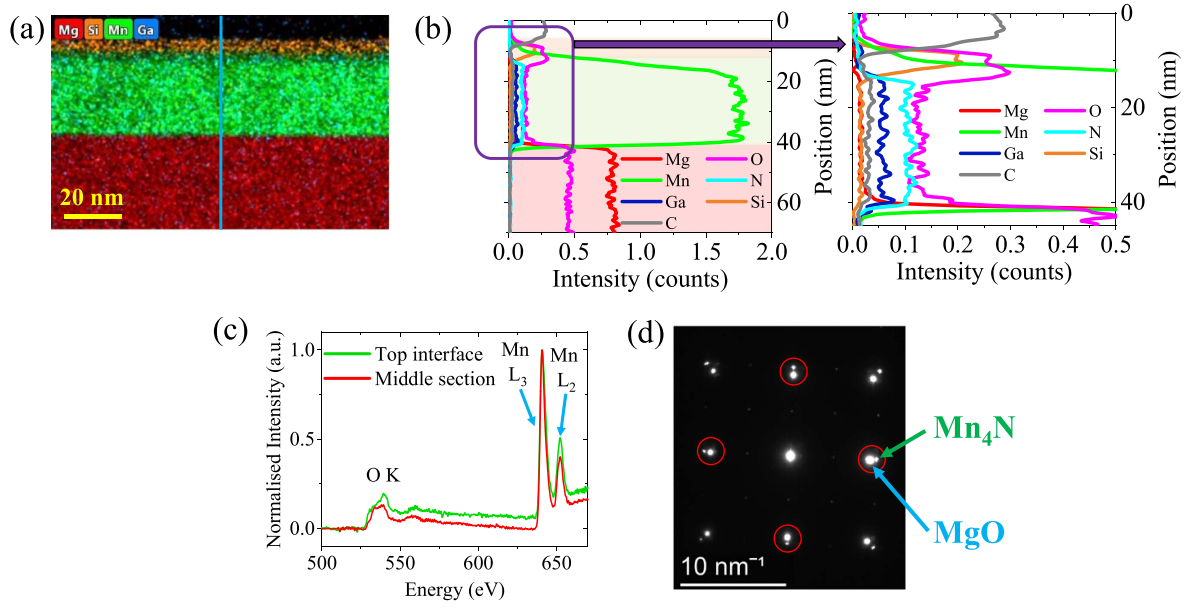
Figure 4. (a) STEM image of the stack structure where the line in blue indicates the profile along which the EDX spectrum in (b) was taken. (c) illustrates EEL spectra from the top interface and middle sections of the film while the SAD pattern of the stack is shown in (d).
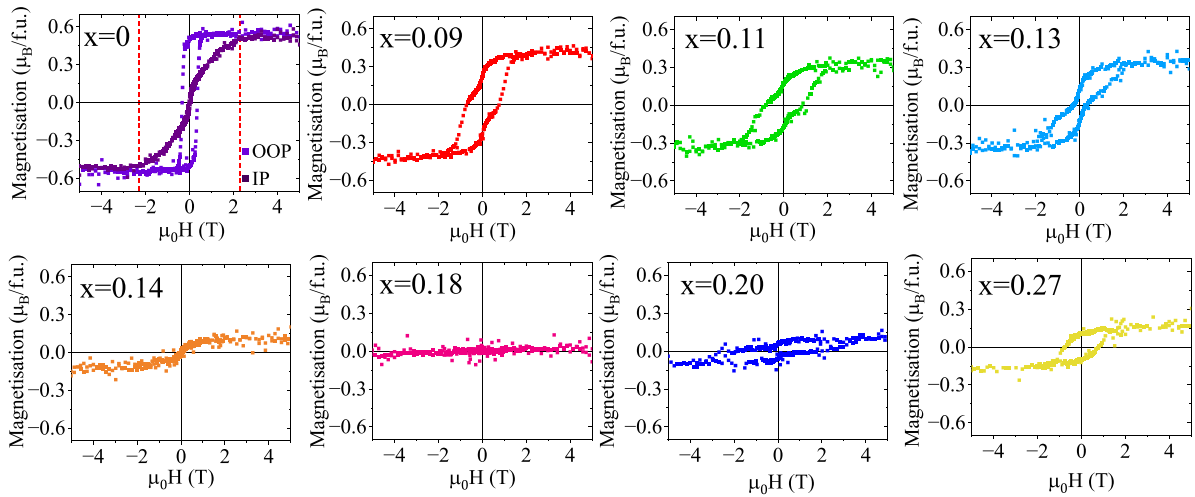

Figure 5. Room temperature SQUID magnetisation loops for $Mn_{4-x}Ga_xN$ thin films. Addition of the nonmagnetic element causes an initial decrease in the saturation magnetisation up to a composition with $x = 0.18$. Further increases in x increase the magnetisation, indicating that $x = 0.18$ is close to the magnetic compensation point. All loops were measured in an out-of-plane orientation but the in-plane (IP) loop is also shown for the undoped film where the dashed red lines on this plot indicate $\mu_0 H_a$.

thin film Mn_4N, $0.56\,\mu_B$/f.u., at room temperature compared to the bulk value of $0.81\,\mu_B$/f.u. [14]. The reason for the lower moment is probably the deformation of the noncollinear 3c sublattice spin structure with PMA, illustrated in figure 1; the average tilt angle $\frac{2\gamma + \delta}{3}$ is lowered as the umbrella-like structure closes slightly towards the easy direction resulting in a greater net 3c moment opposing the dominant 1a moment. Otherwise, a lower nitrogen content in the films could influence the orbital hybridization with Mn 3c. The remanent magnetisation versus temperature curves shown in figure 6(b) indicate one composition ($Mn_{3.82}Ga_{0.18}N$) exhibiting a compensation point in the measured temperature range at 235 K. All curves were measured after field cooling in 5 T to avoid the

paramagnetic signals due to Fe^{3+} or Mn^{2+} impurities in the MgO substrates. For compositions with $x > 0.18$ the remanent magnetisation increases at higher temperatures signifying that the 3c sublattice becomes dominant as more 1a Mn atoms are removed.

All magneto-transport measurements were performed on triple Hall crosses such that the longitudinal and transverse components of the induced voltage could be measured simultaneously. The inset of figure 7(a) shows an optical image of one such bar before the metallisation step. Due to the difficulties encountered in patterning samples smaller than 10×10 mm^2 in area (edge bead formation while spin coating and issues with vacuum retention during patterning),
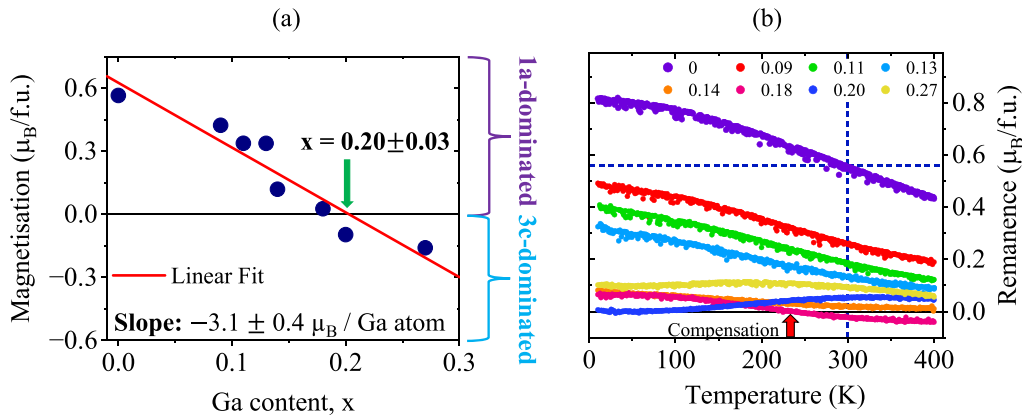
Figure 6. (a) High-field magnetisation as a function of Ga content measured by SQUID magnetometry at 300 K. The moment decrease with increasing Ga-doping confirms that Ga replaces Mn atoms at 1a sites. The remanence is plotted as a function of temperature for each composition in (b), where the dashed blue lines illustrate the moment of 0.56 μ_B/f.u. in the pure sample at 300 K.
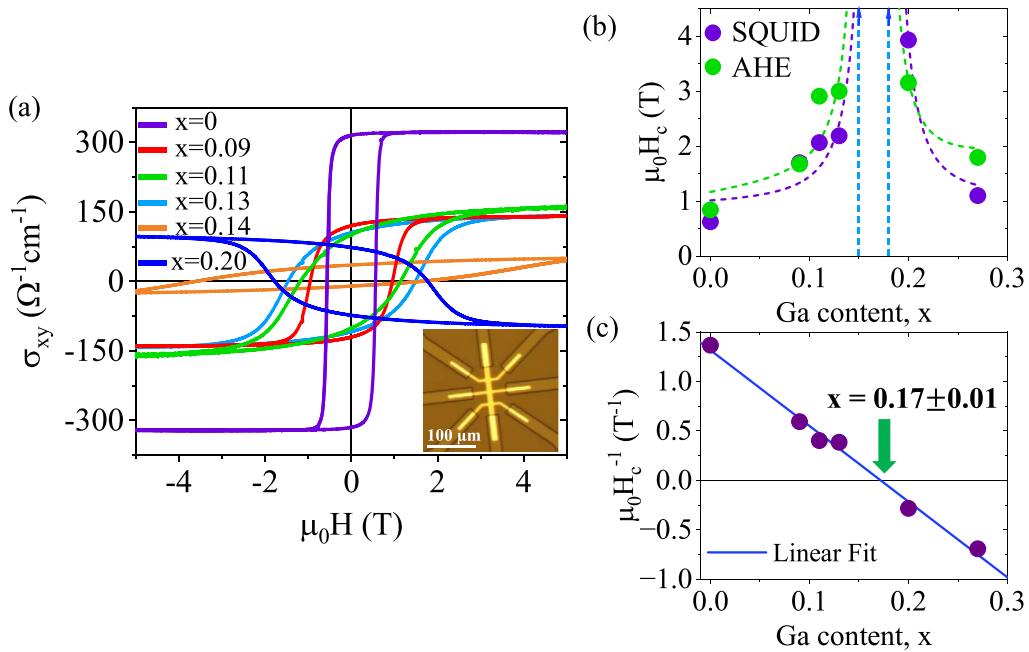

Figure 7. (a) Room temperature AHE loops for six compositions. There is a large initial decrease in σ_{xy} with addition of Ga, then little change but the coercivity increases with x such that the $x = 0.14$ composition cannot be saturated in 5 T. The change in the sign of the AHE and decrease in the coercivity for $x = 0.20$ indicates that compensation has been passed. (b) The room temperature coercive field obtained by SQUID and AHE as a function of Ga content, where the green and purple dotted lines act as a guide to the eye to illustrate the divergence around the compensation composition. A plot of the reciprocal of the average coercive field as a function of Ga doping in (c) intersects the x-axis at compensation.

AHE measurements were performed on different physical samples to those used for SQUID magnetometry. The obtained σ_{xy} loops for six compositions in this series are shown in figure 7(a). There is a strong decrease in the magnitude of the transverse conductivity with the first addition of Ga but further increases in x do not change the saturated σ_{xy} much. This is not the case for the orange loop, $Mn_{3.86}Ga_{0.14}N$, because the coercivity could not be saturated in the maximum field available in our magneto-transport measurement. We observe a systematic increase in the coercivity of these loops with increasing x up to $x = 0.14$, followed by a decrease in the coercivity for $x > 0.20$. The change of sign of the loop for $Mn_{3.80}Ga_{0.20}N$

and the abrupt change in the trend of the coercive field, $\mu_0 H_c$, both indicate that the compensation composition at room temperature is between $x = 0.14$ and $x = 0.20$. We plot the coercive field obtained by SQUID and AHE as a function of Ga content in figure 7(b), where the dotted purple and green lines act as guides to the eye, illustrating the divergence in coercivity. As the SQUID loops are wasp-waisted with hard and soft components, we plot the coercivity of the hard component assuming a square hysteresis loop. In the anomalous Hall effect measurements we also take $\mu_0 H_c$ as the value where the loop closes rather than the field where σ_{xy} changes sign for consistent comparison to the SQUID measurements. There are

slight differences between SQUID and AHE data due to the different samples used in each technique.

In the plot of figure 7(c) the average coercivity from SQUID and AHE measurements was used and its reciprocal crosses zero at $x = 0.17$ when values of $\mu_0 H_c^{-1}$ for compositions $Mn_{3.80}Ga_{0.20}N$ and $Mn_{3.73}Ga_{0.27}N$ are plotted with a negative sign since they are both above compensation and the Mn 3c sublattice then dominates the magnetisation of the system, based on the SQUID loops. This plot indicates room temperature compensation occurs for $x = 0.17 \pm 0.01$, in agreement within the error with the variation in the room temperature magnetic moment. The coercive field seems to be a better indicator of the compensation composition than the magnetic moment. The value of $x = 0.17$ makes more sense when combined with the room temperature magnetisation loops as well as the magnetisation versus temperature curves, where the film with $x = 0.18$ compensates at 235 K. Therefore we expect a composition with a slightly lower value of x than 0.18 to achieve compensation closer to 300 K.

4. Conclusions

The behaviour of thin films of Ga-doped Mn_4N is broadly similar to that of bulk material. Both have triangular ferrimagnetic spin structures. The Ga substitutes preferentially on the 1a corner sites, the majority sublattice in Mn_4N, and reduces the net magnetisation leading to compensation where the two sublattices have equal and opposite net moments, which occurs near room-temperature in films when $x = 0.18$ and in bulk when $x = 0.26$. The main difference is that the bulk material is cubic with weak $\langle 111 \rangle$ anisotropy, $K_1 \approx 1.5 \, \text{kJm}^{-3}$ whereas the thin films have a small tetragonal distortion with $c/a = 0.99$ and strong PMA, $K_1 \approx 100 \, \text{kJm}^{-3}$, with a $\langle 001 \rangle$ easy axis and large coercivity when the net magnetization is small. The frustrated noncollinear magnetic order is modified to decrease the average canting angle $\frac{2\gamma + \delta}{3}$ of the face-center Mn atoms with the magnetic easy axis.

The ability to sputter high-quality films of these materials with PMA and a compensation temperature that can be tailored around room temperature by small changes of the Ga content makes them potentially interesting for spin electronics. Future investigations will focus on the domain structure of the films and on the possibility of a topological Hall effect near compensation, related to the noncollinear ferrimagnetic structure that was reported earlier for the end member [5]. Further work is needed to incorporate $Mn_{4-x}Ga_xN$ into device structures where its magnetisation is pinned by coercivity.

Data availability statement

All data that support the findings of this study are included within the article (and any supplementary files).

Author contributions

L P and P J-C were responsible for sample growth, characterisation and analysis. Y H also contributed to this. A N performed the electron microscopy. K R and Z G helped to direct the work. J M D C conceived and supervised the research and acquired funding for the project. All authors contributed to discussions and the final version of the report. L P drafted this manuscript.

ORCID iDs

L Prendeville ⓘ https://orcid.org/0000-0003-0193-6014
P Jiménez-Cavero ⓘ https://orcid.org/0000-0003-0400-8600
A Naden ⓘ https://orcid.org/0000-0003-2876-6991
Yangkun He ⓘ https://orcid.org/0000-0002-5126-153X
K Rode ⓘ https://orcid.org/0000-0003-2685-6547
Z Gercsi ⓘ https://orcid.org/0009-0003-9743-9609
J M D Coey ⓘ https://orcid.org/0000-0003-0053-8452

References

[1] Finley J and Liu L 2020 Spintronics with compensated ferrimagnets *Appl. Phys. Lett.* **116** 110501

[2] Zhou H-A, Xu T, Bai H and Jiang W 2021 Efficient spintronics with fully compensated ferrimagnets *J. Phys. Soc. Japan* **90** 081006

[3] Kim S K *et al* 2022 Ferrimagnetic spintronics *Nat. Mater.* **21** 24–34

[4] Ghosh S *et al* 2021 Current-driven domain wall dynamics in ferrimagnetic nickel-doped Mn_4N films: very large domain wall velocities and reversal of motion direction across the magnetic compensation point *Nano Lett.* **21** 2580–7

[5] He Y *et al* 2022 Noncollinear ferrimagnetism and anomalous Hall effects in Mn_4N thin films *Phys. Rev.* B **106** L060409

[6] Zhang R, He Y, Fruchart D, Coey J M D and Gercsi Z 2022 Rare-earth-free noncollinear metallic ferrimagnets $Mn_{4-x}Z_xN$ with compensation at room temperature *Acta Mater.* **234** 118021

[7] Li C *et al* 2008 Fabrication and magnetic characteristic of ferrimagnetic bulk Mn_4N *J. Alloys Compd.* **457** 57–60

[8] Yasuda T *et al* 2023 Sign reversal in anomalous Hall effect at two Sn compositions in $Mn_{4-x}Sn_xN$ films on MgO(001) substrates *AIP Adv.* **13** 015119

[9] Komori T *et al* 2019 Magnetic and magneto-transport properties of Mn_4N thin films by Ni substitution and their possibility of magnetic compensation *J. Appl. Phys.* **125** 213902

[10] Mitarai H *et al* 2020 Magnetic compensation at two different composition ratios in rare earth free $Mn_{4-x}Co_xN$ ferrimagnetic films *Phys. Rev. Mater.* **4** 094401

[11] Komori T *et al* 2022 Magnetic structure of 3d-element doped Mn_4N films confirmed by X-ray magnetic circular

dichroism—conditions for magnetic compensation *J. Magn. Magn. Mater.* **564** 170050

[12] Yasuda T *et al* 2022 Ferrimagnetic–ferromagnetic phase transition in Mn$_4$N films favored by non-magnetic In doping *J. Phys. D: Appl. Phys.* **55** 115003

[13] Sakaguchi H, Isogami S, Niimi M and Ishibashi T 2023 Boron-induced magneto-optical Kerr spectra and dielectric tensors in ferrimagnetic (Mn$_4$N)B antiperovskite thin films *J. Phys. D: Appl. Phys.* **56** 365002

[14] Fruchart D, Givord D, Convert P, l'Heritier P and Senateur J P 1979 The non-collinear component in the magnetic structure of Mn$_4$N *J. Phys. F: Met. Phys.* **9** 2431–7

[15] Uhl M, Matar S F and Mohn P 1997 Ab initio analysis of magnetic properties in noncollinearly ordered Mn$_4$N *Phys. Rev.* B **55** 2995–3002

[16] Yasutomi Y, Ito K, Sanai T, Toko K and Suemasu T 2014 Perpendicular magnetic anisotropy of Mn$_4$N films on MgO(001) and SrTiO$_3$(001) substrates *J. Appl. Phys.* **115** 17A935

[17] Hirose T *et al* 2020 Strong correlation between uniaxial magnetic anisotropic constant and in-plane tensile strain in Mn$_4$N epitaxial films *AIP Adv.* **10** 025117

[18] Hirose T, Komori T, Gushi T, Toko K and Suemasu T 2020 Perpendicular magnetic anisotropy in ferrimagnetic Mn$_4$N films grown on (LaAlO$_3$)$_{0.3}$(Sr$_2$TaAlO$_6$)$_{0.7}$(001) substrates by molecular beam epitaxy *J. Cryst. Growth* **535** 125566

[19] Ching K M, Chang W D, Chin T S, Duh J G and Ku H C 1994 Anomalous perpendicular magnetoanisotropy in Mn$_4$N films on Si(100) *J. Appl. Phys.* **76** 6582–4

[20] Suemasu T, Vila L and Attané J-P 2021 Present status of rare-earth free ferrimagnet Mn$_4$N and future prospects of Mn$_4$N-based compensated ferrimagnets *J. Phys. Soc. Japan* **90** 081010

[21] Zhang Z and Mi W 2022 Progress in ferrimagnetic Mn$_4$N films and its heterostructures for spintronics applications *J. Phys. D: Appl. Phys.* **55** 013001

[22] Coey J M D, Givord D and Fruchart D 2022 Metallic Nitride and Carbide Perovskites: history and prospects *ECS J. Solid State Sci. Technol.* **11** 055002

[23] Momma K and Izumi F 2011 VESTA 3 for three-dimensional visualization of crystal, volumetric and morphology data *J. Appl. Crystallogr.* **44** 1272–6

[24] Bayaraa T, Xu C and Bellaiche L 2021 Magnetization compensation temperature and frustration-induced topological defects in ferrimagnetic antiperovskite Mn$_4$N *Phys. Rev. Lett.* **127** 217204

[25] Gercsi Z, He Y and Coey J M D 2023 Comment on magnetization compensation temperature and frustration-induced topological defects in ferrimagnetic antiperovskite Mn$_4$N *Phys. Rev. Lett.* **131** 089701

[26] Mandru A-O *et al* 2020 Pervasive artifacts revealed from magnetometry measurements of rare earth-transition metal thin films *J. Vac. Sci. Technol.* A **38** 023409

[27] Miller A M *et al* 2022 Extracting information from x-ray diffraction patterns containing Laue oscillations *Z. Naturforsch.* B **77** 313–22

[28] Takei W J, Heikes R R and Shirane G 1962 Magnetic Structure of Mn$_4$N-Type Compounds *Phys. Rev.* **125** 1893–7

[29] Shen X *et al* 2014 Metallic transport and large anomalous Hall effect at room temperature in ferrimagnetic Mn$_4$N epitaxial thin film *Appl. Phys. Lett.* **105** 072410

[30] Gushi T *et al* 2018 Millimeter-sized magnetic domains in perpendicularly magnetized ferrimagnetic Mn$_4$N thin films grown on SrTiO$_3$ *Jpn. J. Appl. Phys.* **57** 120310

[31] Isogami S, Masuda K and Miura Y 2020 Contributions of magnetic structure and nitrogen to perpendicular magnetocrystalline anisotropy in antiperovskite ε-Mn$_4$N *Phys. Rev. Mater.* **4** 014406

[32] Li W *et al* 2022 Growth of Mn$_4$N film with enhanced perpendicular magnetization on glass substrate using MnO seed layer *Mater. Lett.* **311** 131615

[33] Schmid H and Mader W 2006 Oxidation states of Mn and Fe in various compound oxide systems *Micron* **37** 426–32

[34] Li H *et al* 2018 Suppression of anomalous Hall effect by heavy-fermion in epitaxial antiperovskite Mn$_{4-x}$Gd$_x$N films *J. Appl. Phys.* **124** 093903